Progress In Electromagnetics Research C, Vol. 99, 1–14, 2020

Coherence Reduction of the Measurement Matrix in Microwave Computational Imaging by Introducing Polarization Diversity

Jian Guan, Chang Chen, and Weidong Chen*

Abstract—For microwave computational imaging (MCI), the reduction of measurement matrix's coherences permits better reconstruction performance. Therefore, frequency diverse apertures (FDAs) have become a major option of antennas for MCI due to thier frequency-varying radiation patterns. The frequency diversity in the patterns reduces coherences; however, the losses in practical materials and the finite sizes of apertures impose upper limits on frequency diversity. For further coherence reduction, the polarization diversity (PD) of aperture elements is as a new approach introduced in this paper. We present an electromagnetic formulation of scattering aperture elements' PD. In the formulation, the PD brings an additional degree of freedom in the generation of the measurement matrix, given the apertures being illuminated with varying polarizations. This new degree of freedom enables a potential of reducing the coherences. Two complementary electric-field-coupled (cELC) scattering apertures, which differentiate in the polarizations of elements, are fabricated for validation. A set of comparisons yielded by the near-field scanning data of these apertures shows that the PD effectively reduces coherences and improves reconstruction performance.

1. INTRODUCTION

MCI is a new microwave imaging paradigm that retrieves probed objects' spatial information via a set of indirect measurements generated by the radiated fields of antennas. The measurements transfer the burden of reconstruction from beam formation in conventional microwave imaging to modelling and post processing in MCI [1]. The additional flexibility gives a great advantage of simplifying hardware complexity and getting rid of mechanical movements [2]. Therefore, MCI has become a research focus in the field of microwave imaging in recent years.

Basically, MCI shares the same model with inverse scattering imaging, considering the combination of the electric-field integral equation and the reciprocity of receiving antennas [3]. Under the first-order Born approximation, MCI solves a linear Fredholm integral equation of the first kind (i.e., a linear integral operator), of which the integral kernel is composed of the measurements [4]. The integral operator transforms scene information from the object space to the measurement space [5]. Since the reconstruction is to inverse the transformation, the measurements plays an important role in determining imaging performance. In discrete form, the Fredholm integral equation leads to a matrix equation, in which the coefficient matrix, usually noted as the measurement matrix or the sensing matrix, is composed of the measurements in discrete form. It is worth mentioning that, as a finite-dimensional duplicate, the measurement matrix shares the same properties with the integral operator. For convenience in expression, the matrix form is preferred.

As with other typical inverse problems, insufficient bases spanning the measurement space result in the ill-posedness which impedes the reconstruction of objects, thus making the number of the

Received 7 October 2019, Accepted 6 January 2020, Scheduled 17 January 2020
* Corresponding author: Weidong Chen (wdchen@ustc.edu.cn).
The authors are with the Key Laboratory of Electromagnetic Space Information, University of Science and Technology of China, China.

measurement bases a critical factor. In [5], a positive relationship between spatial resolution and the number of independent measurements in a MCI system is presented. Obviously, reducing the mutual coherences in the measurement matrix is a necessary condition to enlarge the number of the bases. High coherences imply that there are massive redundant measurements applying to the object with tiny differences, occupying the amount of measurement energy but bringing very few information. In addition, some researchers also related coherences to the maximum sidelobe level of the imaging system [6]. Therefore, reducing the mutual coherences in the measurement matrix has become a key challenge for the design of a MCI system.

Since the measurements are implemented by radiated fields, the antennas determine the coherence level of the measurement matrix. FDA with frequency-diverse radiation patterns is first proposed to generate low-coherent measurements required by MCI [7–9]. For a MCI system with a FDA, a set of measurements is performed by a frequency sweep, encoding the spatial information into the S-parameters via the "quasi-random" radiation patterns generated by the aperture, of which the elements are configured with random resonant frequencies. The frequency sweep immensely simplifies the complexity in the implementation of measurements, and the frequency diversity of the radiation patterns effectively reduces the mutual coherences in the measurement matrix, thus making FDA a major option of antennas for MCI.

For FDA, the frequency diversity of radiation patterns is determined by the frequency diversity of element excitations. In addition to the random configuration of element resonant frequencies, most FDAs also introduce randomness or chaos into the resonant cavities, such as the mode-mixing cavity structure [10] and the printed metasurface with subwavelength metallic cylinders in the cavity [11]. The stationary waves perturbed in the cavities stimulate the elements, leading to randomized or diversified excitations. The introduced frequency diversity of the cavity modes shares responsibility for the generation of radiation diversity together with the elements. FDA achieves a proper balance between the coherence reduction and hardware complexity; however, the excitation diversity requires sharp and sensitive frequency responses, which makes high quality (Q) factors a necessary condition for the coherence reduction [12]. This leads to an arduous pursuit of high Q factors due to its difficulty in implementation with limited aperture sizes and practical lossy materials. New approaches that bring diversity in the excitations of aperture elements are therefore much needed.

The emergence of dynamic metasurface, in 2015, which is composed of radiating elements mounted with electric reconfigurable components, offers another option for MCI [13]. Dynamic apertures enlarge the diversity by controlling the voltage applied to the reconfigurable components, which makes the radiating status of the elements vary accordingly, and thus results in a set of encoded reconfigurable radiation patterns. The dynamic apertures possess great advantages in radiation diversity due to the tremendous degrees of freedom in aperture configurations, however at the expense of an additional complexity of the reconfigurable components. In 2016, some researchers achieved "abundance improvement" in the measurements by rotating the aperture in a MCI system [14]. The rotation significantly reduces the mutual coherences in the measurements, improving the imaging performance at the expense of a simple mechanical movement. This illuminating work implies that mechanical rotations can be a practicable approach to the coherence reduction at an acceptable cost. Recently, a very innovative aperture with reconfigurable chaotic cavity was proposed, in which the boundary of the cavity is tuned by switching on/off the fluorescent lamps inserted into the cavity as reconfigurable plasma scatters [15]. The switching status of the lamps brings additional degrees of freedom in the generation of the excitation diversity, which therefore relaxes the requirement of high Q factors.

In a similar way to the above-mentioned approaches, element polarizations, as configurable variables of apertures, also possess a potential of offering additional degrees of freedom in the generation of the measurements. In 2018, a frequency-polarization-diverse aperture (FPDA) is proposed for MCI [16], which is the first time the PD of aperture elements is taken into consideration for the coherence reduction. The FPDA is a reflective aperture that is composed of polarization sensitive cells with different resonant frequencies and polarization arrangements, thus generating more uncorrelated measurements when rotating the aperture under a fixed illumination. However, the researchers did not implement further investigation on the formulation of the PD's benefit, leaving a research gap about this issue. According to [17], antenna's polarizations at most double the electromagnetic degree of freedom for a two-dimensional (2D) imaging scenario, which permits more information being interrogated via

measurements. Therefore, this research gap is well worth investigating.

The intention of this paper is to give an electromagnetic formulation of aperture elements' PD and investigate its benefit in the coherence reduction of the measurement matrix. In the 2D imaging scenario under consideration, we illuminate a fixed scattering FDA composed of arbitrarily polarized elements with vertically and horizontally polarized plane waves respectively, in order to conveniently alter the intensity of element excitations via the polarization of illumination. By modeling the aperture into an electric dipole expansion, we formulate the generation of the measurements with the PD being an independent variable. The formulation shows that the emergence of the PD brings an additional degree of freedom in the measurements when altering the polarization of illumination, thus enabling a potential of reducing the coherences in the measurement matrix. Two cELC scattering apertures which only differentiate in the polarization of elements (with or without PD) are fabricated for validation. A set of comparisons yielded by the near-field scanning data obtained in a microwave anechoic chamber validates that under the illuminations with varying polarizations, the PD is capable of significantly reducing the mutual coherences in the measurement matrix, and thus improves the reconstruction performance of MCI.

This paper is organized as follows. In Section 2, we briefly introduce the imaging model of MCI, and then give the electromagnetic formulation. The validation of the proposed formulation is demonstrated in Section 3, where the comparisons are also presented. In the end, the conclusions are given in Section 4.

2. THEORY

In this section, a brief review of the electromagnetic model of MCI is presented as a prelude, then we give the electromagnetic formulation of the PD's influence on the measurement matrix's coherences.

2.1. Electromagnetic Model of MCI

The 2D imaging scenario under consideration is shown in Figure 1, where an arbitrary scattering array aperture is placed as a transmitting/receiving antenna stimulated by the illumination of plane waves.

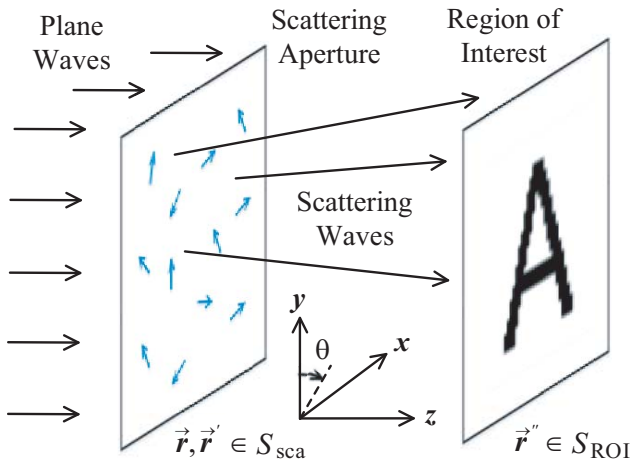

Figure 1. Imaging scenario under consideration.

In this scenario, the scattering aperture represents an idealized model of a scattering structure which is composed of lossless dielectric materials and perfectly conducting objects. The region of interest (ROI) where the probed object (the capital letter 'A') is located is illuminated by the scattering fields of the scattering aperture. S_{sca} and S_{ROI} denote the region of the scattering aperture and the ROI, respectively. It should be noted that the configuration in the scenario is specifically modified for our following formulation of the PD, while in the general MCI model the scattering aperture and the plane-wave illumination are replaced with general transmitting/receiving antennas.

When an object in the ROI is under the illumination radiated from the transmitting aperture, the induced currents of the object act equivalently as a secondary radiation source, scattering back to the receiving aperture. Ignoring the scattering from the receiving aperture, the reciprocity of antennas yield the echoes by the dot product of the scattering field radiated from the object and the virtual electric current of the receiving aperture when it is used for transmitting. Combined with the reciprocity of Green's function in free space, the above-mentioned process formulates the electromagnetic model of MCI as a nonlinear Fredholm integral equation of the first kind [3]:

$$g = \mathcal{H}x := -\frac{\mathrm{j}k_0}{Z_0}\int_{S_{\mathrm{ROI}}}\left[\varepsilon_{\mathrm{r}}\left(\vec{\mathbf{r}}''\right) - \frac{\mathrm{j}\sigma\left(\vec{\mathbf{r}}''\right)}{\omega\varepsilon_0} - 1\right]\vec{\mathbf{E}}\left(\vec{\mathbf{r}}''\right)\cdot\vec{\mathbf{E}}_{\mathrm{Rx}}\left(\vec{\mathbf{r}}''\right)\mathrm{d}^2\vec{\mathbf{r}}'' \tag{1}$$

where g is the echo; $\mathcal{H}$ is the integral operator; $x{:=}\varepsilon_{\mathrm{r}}(\vec{\mathbf{r}}'') - \mathrm{j}\sigma(\vec{\mathbf{r}}'')/\omega\varepsilon_0 - 1$ is the "contrast function" of the object; k_0 and Z_0 are the spatial frequency and the wave impedance in free space; ε_{r} and σ are the relative permittivity and the conductivity of the object; $\vec{\mathbf{E}}$ is the total field excited by the incident field $\vec{\mathbf{E}}_{\mathrm{inc}}$; and $\vec{\mathbf{E}}_{\mathrm{Rx}}$ is the virtual field when the receiving antenna is excited by a normalized feed. It is worth mentioning that Equation (1) can also be yielded via the volume integral equation in inverse scattering problems combined with the formulation of the receiving antenna. From the view of inverse scattering imaging, MCI shares the same formulation, but additionally considering the reciprocity of receiving antennas.

In Equation (1), the object is represented by x, which is the objective of reconstruction. The integral shows that the object is sampled by the "measurement mode" h, which is defined as the dot product of the fields $\vec{\mathbf{E}}\cdot\vec{\mathbf{E}}_{\mathrm{Rx}}$. Ignoring the constants in Equation (1), the "measurement matrix" $\overline{\overline{\mathbf{H}}}$ can be yielded as $\mathcal{H}$ in finite-dimensional form. The rows of $\overline{\overline{\mathbf{H}}}$ are composed ofe h that is discrete in the ROI, while each row corresponds to a measurement. For most MCI applications where measurements are implemented by a frequency sweep, the number of rows equals the number of the sweep points. The inverse of $\overline{\overline{\mathbf{H}}}$ leads to the reconstruction of the object; however, it inevitably encounters two difficulties: the nonlinearity between x and h, and the ill-posedness in the nature of inverse problems.

The integral kernel in Equation (1), i.e., the measurement mode $h := \vec{\mathbf{E}}\cdot\vec{\mathbf{E}}_{\mathrm{Rx}}$, is a nonlinear function of x, thus bringing nonlinearity to the reconstruction of the object. The presence of the object perturbs $\vec{\mathbf{E}}$ in the ROI makes $\vec{\mathbf{E}}$ diverse from $\vec{\mathbf{E}}_{\mathrm{inc}}$. The perturbation is the root cause of the nonlinearity. The first-order Born approximation which replaces $\vec{\mathbf{E}}$ with $\vec{\mathbf{E}}_{\mathrm{inc}}$ is only applicable to weak-scattering objects. For most inverse scattering problems where the object of interest is of electrically "high-density" and is comparable in size with wavelength, the nonlinearity is non-ignorable and should be solved by nonlinear approaches such as Born iterative method [18] and contrast source inversion [19]. However, in microwave imaging applications where the object is relatively large compared with the wavelength, the first-order Born approximation maintains acceptable accuracy for reconstruction, because the object's spatial details in the scale of wavelength/sub-wavelength are beyond the scope of the imaging of electrically large objects [20]. Therefore, the first-order Born approximation is adopted in our formulation, which makes H a linear operator and thus linearizes the reconstruction. For the rest of this paper, $\mathcal{H}$ and $\overline{\overline{\mathbf{H}}}$ are respectively regarded as a linear operator and a linear matrix of x by default.

The operator $\mathcal{H}$ is compact since h is a smooth and bounded function. However, the inverse of $\mathcal{H}$ is non-compact due to the unbounded eigenvalues of the inverse operator [21], which brings ill-posedness to the reconstruction. In matrix form, the ill-posedness leads to rank deficiency of $\overline{\overline{\mathbf{H}}}$, making its inverse unstable in the presence of noise and hence deterring the reconstruction. In order to ameliorate the ill-posedness, it is crucial to orthogonalize the measurements and enlarge the number of the bases spanning the measurement space, which necessarily requires to minimize the mutual coherences between the measurement modes:

$$\min\left\langle h_i\left(\vec{\mathbf{r}}''\right)\ h_j\left(\vec{\mathbf{r}}''\right)\right\rangle \text{ for } i \neq j \tag{2}$$

In Equation (2), angle bracket $\langle\,\rangle$ denotes the coherence calculation.

As previously introduced, FDA is a major option of antennas for MCI due to its frequency-varying "quasi-random" radiation patterns. It would be of great interest if there are other approaches reducing the coherences without extra heavy burden on hardwares. The PD of aperture elements gives diverse

radiation patterns under proper illuminations, which just meets the requirement. Next, we will formulate the PD's influence on the coherences.

3. FORMULATION OF THE POLARIZATION DIVERSITY

In order to explicitly formulate the influence of the PD, we start with the relationship between the radiated fields in the ROI and apertures. This is intended to relate the polarization arrangement of the aperture elements shown in Figure 1 to the measurement mode h. By utilizing the spatial spectral expansion of Green's dyad in [22], the authors of [3] formulate h with the spatial spectrum of aperture's equivalent radiation source (i.e., the source in k-space). It shows that the fields in the Fraunhofer region of a radiation source can be yielded by the source's spectrum at a stationary point in the k-space. In other words, the space in Fraunhofer region is bijective to the k-space, decomposing the fields in the ROI into a set of plane waves. This relationship can be extended to a more general situation, in which Fresnel diffraction corresponds to a fractional Fourier transform of radiation sources, and it evolves to a conventional Fourier transform with the range increasing into Fraunhofer region (details can be found in [23, 24]).

According to [3], by utilizing the bijective relationship, h can be formulated with the source's spectrum which is constrained by a spectral low-pass filter formed by the finite angle of view (AOV) in the scenario:

$$h\left(\vec{\mathbf{r}}''\right) \propto \left[\tilde{\vec{\mathbf{J}}}_{\mathrm{m}}^{\mathrm{Tx}}\left(\vec{\mathbf{k}}_{xy}\right) \cdot \tilde{\vec{\mathbf{J}}}_{\mathrm{m}}^{\mathrm{Rx}}\left(\vec{\mathbf{k}}_{xy}\right)\right]_{\vec{\mathbf{k}}_{xy}(\vec{\mathbf{r}}'')\in \mathrm{LPF}} \tag{3}$$

where $\vec{\mathbf{J}}_{\mathrm{m}}$ is the equivalent magnetic current density of the scattering aperture under illuminations; subscript LPF denotes the low-pass filter; Tx and Rx denote transmitting and receiving, respectively; and the tilde denotes the 2D spectrum in the transverse dimensions x-y.

Magnetic current $\vec{\mathbf{J}}_{\mathrm{m}}$ arises from the aperture elements being illuminated by the plane waves, and it appears as a result of electromagnetic equivalence theorem. Equation (3) is formulated as a function of magnetic currents due to the convenience in formulation of most apertures applied for MCI with complementary structures. This does not reduce the generality of our formulation, since another form of Equation (3) with electric currents being a variable can be found in [3], and similar results can be obtained via electromagnetic duality.

Equation (3) implies that the PD's influence on h can be formulated with $\vec{\mathbf{J}}_{\mathrm{m}}$ being modeled as a function of aperture element polarizations. Generally, $\vec{\mathbf{J}}_{\mathrm{m}}$ can be yielded by the dot product of magnetic susceptibility $\overleftrightarrow{\chi}_{\mathrm{m}}$ and magnetic field $\vec{\mathbf{H}}$, while for an aperture fabricated with dielectric, magnetic and perfectly conducting objects in electrically small dimensions, the aperture can be approximated by a dipole expansion [25]. Most apertures applied to MCI are composed of radiating elements in sub-wavelength scales, thus making the dipole expansion a good assumption. Hence, the aperture's equivalent magnetic susceptibility $\overleftrightarrow{\chi}_{\mathrm{m}}$ can be replaced with $f\hat{\mathbf{p}}_{\mathrm{cell}}\hat{\mathbf{p}}_{\mathrm{cell}}$, where f is the frequency response of the approximated dipole, and $\hat{\mathbf{p}}_{\mathrm{cell}}$ is the unit vector of its polarization. Then it gives:

$$\vec{\mathbf{J}}_{\mathrm{m}}\left(\vec{\mathbf{r}}\right) \approx -\mathrm{j}\omega\mu_0\Delta s^{-1}\overleftrightarrow{\chi}_{\mathrm{m}}\left(\vec{\mathbf{r}}\right) \cdot \vec{\mathbf{H}}\left(\vec{\mathbf{r}}\right) \approx -\mathrm{j}\omega\mu_0\Delta s^{-1} f\left(\vec{\mathbf{r}}\right) \hat{\mathbf{p}}_{\mathrm{cell}}\left(\vec{\mathbf{r}}\right) \hat{\mathbf{p}}_{\mathrm{cell}}\left(\vec{\mathbf{r}}\right) \cdot \vec{\mathbf{H}}\left(\vec{\mathbf{r}}\right) \tag{4}$$

where Δs is the discrete area of a dipole.

Recall the formulation of the scattering field $\vec{\mathbf{H}}_{\mathrm{sca}}$ by the integral of a Green's dyad $\overleftrightarrow{\mathbf{G}}$ and $\vec{\mathbf{J}}_{\mathrm{m}}$:

$$\vec{\mathbf{H}}_{\mathrm{sca}}\left(\vec{\mathbf{r}}\right) = \mathrm{j}\omega\varepsilon_0 \int_{S_{\mathrm{sca}}} \overleftrightarrow{\mathbf{G}}\left(\vec{\mathbf{r}}, \vec{\mathbf{r}}'\right) \cdot \vec{\mathbf{J}}_{\mathrm{m}}\left(\vec{\mathbf{r}}'\right) \mathrm{d}^2\vec{\mathbf{r}}' \tag{5}$$

Considering that the total field $\vec{\mathbf{H}}$ is composed of $\vec{\mathbf{H}}_{\mathrm{inc}}$ (i.e., the plane-wave illumination) and $\vec{\mathbf{H}}_{\mathrm{sca}}$, the combination of Equations (4) and (5) gives a linear relationship between the polarization of $\vec{\mathbf{H}}_{\mathrm{inc}}$ and $\vec{\mathbf{H}}$:

$$\hat{\mathbf{p}}_{\mathrm{inc}}\left(\vec{\mathbf{r}}\right) \propto \int_{S_{\mathrm{sca}}} \left[\delta\left(\vec{\mathbf{r}} - \vec{\mathbf{r}}'\right) \overleftrightarrow{\mathbf{I}} - \Delta s^{-1} k_0^2 f\left(\vec{\mathbf{r}}'\right) \overleftrightarrow{\mathbf{G}}\left(\vec{\mathbf{r}}, \vec{\mathbf{r}}'\right) \cdot \hat{\mathbf{p}}_{\mathrm{cell}}\left(\vec{\mathbf{r}}'\right) \hat{\mathbf{p}}_{\mathrm{cell}}\left(\vec{\mathbf{r}}'\right)\right] \cdot \vec{\mathbf{H}}\left(\vec{\mathbf{r}}'\right) \mathrm{d}^2\vec{\mathbf{r}}' = \left(\mathcal{T}_{\mathrm{sca}}\vec{\mathbf{H}}\right)\left(\vec{\mathbf{r}}\right) \tag{6}$$

where $\hat{\mathbf{p}}_{\mathrm{inc}}$ is the unit vector of $\vec{\mathbf{H}}_{\mathrm{inc}}$; δ is a Dirac delta function; and $\mathcal{T}_{\mathrm{sca}}$ is the operator of this integral. It should be noted that $\vec{\mathbf{H}}_{\mathrm{inc}}$ has been replaced with $\hat{\mathbf{p}}_{\mathrm{inc}}$ in Equation (6) with the intention of highlighting

the polarization as an independent variable. The replacement does not affect the formulation since the amplitude and the phase of $\vec{\mathbf{H}}_{\text{inc}}$ only contribute to a complex constant in the equation.

In order to apply Equations (6) to (4), an inversion of $\mathcal{T}_{\text{sca}}$ is needed, which gives:

$$\vec{\mathbf{H}}\left(\vec{\mathbf{r}}\right) \propto \left(\mathcal{T}_{\text{sca}}^{\dagger}\hat{\mathbf{p}}_{\text{inc}}\right)\left(\vec{\mathbf{r}}\right) \tag{7}$$

where $\mathcal{T}_{\text{sca}}^{\dagger}$ is the inverse operator of $\mathcal{T}_{\text{sca}}$. Combining Equation (7) with (4) leads to:

$$\vec{\mathbf{J}}_{\text{m}}\left(\vec{\mathbf{r}}\right) \propto -\text{j}\omega\mu_0\Delta s^{-1} f\left(\vec{\mathbf{r}}\right)\hat{\mathbf{p}}_{\text{cell}}\left(\vec{\mathbf{r}}\right)\hat{\mathbf{p}}_{\text{cell}}\left(\vec{\mathbf{r}}\right)\cdot\left(\mathcal{T}_{\text{sca}}^{\dagger}\hat{\mathbf{p}}_{\text{inc}}\right)\left(\vec{\mathbf{r}}\right) \tag{8}$$

Since $\hat{\mathbf{p}}_{\text{cell}}$ is determined by aperture element polarizations, Equation (8) formulates the relationship between $\vec{\mathbf{J}}_{\text{m}}$ and the element polarizations under the illumination of $\hat{\mathbf{p}}_{\text{inc}}$. The PD of the aperture is then defined as the spatial diversity of $\hat{\mathbf{p}}_{\text{cell}}$.

Before we relate Equation (8) to (3), it would be convenient to define the following functions with the purpose of yielding a concise formulation:

$$\begin{aligned}
\hat{\mathbf{p}}_{\text{cell}}\left(\vec{\mathbf{r}}\right) &= \left[\ \cos\theta_{cell}\left(\vec{\mathbf{r}}\right) \quad \sin\theta_{cell}\left(\vec{\mathbf{r}}\right)\ \right] \\
\left(\mathcal{T}_{\text{sca}}^{\dagger}\hat{\mathbf{p}}_{\text{inc}}\right)\left(\vec{\mathbf{r}}\right) &= H_{\text{inc}}^{\dagger}\left(\vec{\mathbf{r}}\right)\left[\ \cos\theta_{inc}^{\dagger}\left(\vec{\mathbf{r}}\right) \quad \sin\theta_{inc}^{\dagger}\left(\vec{\mathbf{r}}\right)\ \right]^{\text{T}} \\
P\left(\vec{\mathbf{r}},\hat{\mathbf{p}}_{\text{inc}}\right) &:= \hat{\mathbf{p}}_{\text{cell}}\left(\vec{\mathbf{r}}\right)\cdot\left(\mathcal{T}_{\text{sca}}^{\dagger}\hat{\mathbf{p}}_{\text{inc}}\right)\left(\vec{\mathbf{r}}\right) = H_{\text{inc}}^{\dagger}\left(\vec{\mathbf{r}},\hat{\mathbf{p}}_{\text{inc}}\right)\cos\left[\theta_{\text{cell}}-\theta_{\text{inc}}^{\dagger}\right]\left(\vec{\mathbf{r}},\hat{\mathbf{p}}_{\text{inc}}\right)
\end{aligned} \tag{9}$$

where all the polarization vectors are expressed in terms of angle θ which is defined in x-y plane as shown in Figure 1, and $\mathcal{T}_{\text{sca}}^{\dagger}\hat{\mathbf{p}}_{\text{inc}}$ is then decomposed into the amplitude $H_{\text{inc}}^{\dagger}$ and the unit vector $[\ \cos\theta_{\text{inc}}^{\dagger} \quad \sin\theta_{\text{inc}}^{\dagger}\ ]^{\text{T}}$. It should be noted that $\cos\theta$ and $\sin\theta$ are spatial functions varying over the aperture. Consequently, a function P, which indicates the excitation intensity of a dipole and thus embodies the PD, can be defined as shown in Equation (9). Combining with Equation (9), applying 2D spatial Fourier transformation F_{2D} in the transverse dimensions to Equation (8) yields:

$$\tilde{\vec{\mathbf{J}}}_{\text{m}}\left(\vec{\mathbf{k}}_{xy},\hat{\mathbf{p}}_{\text{inc}}\right) \propto \omega\tilde{f}\left(\vec{\mathbf{k}}_{xy}\right) * \tilde{P}\left(\vec{\mathbf{k}}_{xy},\hat{\mathbf{p}}_{\text{inc}}\right) * \left[\ \tilde{\cos}\theta_{cell}\left(\vec{\mathbf{k}}_{xy}\right) \quad \tilde{\sin}\theta_{cell}\left(\vec{\mathbf{k}}_{xy}\right)\ \right]^{\text{T}} \tag{10}$$

where $*$ denotes convolution in the k-space, and:

$$\tilde{P}\left(\vec{\mathbf{k}}_{xy},\hat{\mathbf{p}}_{\text{inc}}\right) = \tilde{H}_{\text{inc}}^{\dagger}\left(\vec{\mathbf{k}}_{xy},\hat{\mathbf{p}}_{\text{inc}}\right) * \tilde{\cos}\left[\theta_{\text{cell}}-\theta_{\text{inc}}^{\dagger}\right]\left(\vec{\mathbf{k}}_{xy},\hat{\mathbf{p}}_{\text{inc}}\right) \tag{11}$$

$$\tilde{\cos}\,\theta\left(\vec{\mathbf{k}}_{xy}\right) := \left(\text{F}_{\text{2D}}\cos\theta\right)\left(\vec{\mathbf{k}}_{xy}\right) \tag{12}$$

$$\tilde{\sin}\,\theta\left(\vec{\mathbf{k}}_{xy}\right) := \left(\text{F}_{\text{2D}}\sin\theta\right)\left(\vec{\mathbf{k}}_{xy}\right) \tag{13}$$

Generally, $\theta_{\text{inc}}^{\dagger}$ is determined by both $\vec{\mathbf{H}}_{\text{inc}}$ and the elements, as stated in Equation (7). However, for most apertures composed of weak-scattering elements, the polarization angle of $\hat{\mathbf{p}}_{\text{inc}}$ is a good approximation to $\theta_{\text{inc}}^{\dagger}$. The exact determination of $\vec{\mathbf{H}}$, as another inverse problem irrelevant to our formulation, is beyond the scope of this paper.

Apply Equation (10) to (3), then it yields h as a function with $\tilde{P}$:

$$\begin{aligned}
h\left(\vec{\mathbf{r}}'',\hat{\mathbf{p}}_{\text{inc}}\right) \propto\ & \left[\tilde{\vec{\mathbf{J}}}_{\text{m}}^{\text{Tx}}\left(\vec{\mathbf{k}}_{xy}\right)\cdot\tilde{\vec{\mathbf{J}}}_{\text{m}}^{\text{Rx}}\left(\vec{\mathbf{k}}_{xy}\right)\right]_{\text{LPF}} \\
\propto\ & \omega^2\left\{\left[\tilde{f}_{\text{Tx}}\left(\vec{\mathbf{k}}_{xy}\right) * \tilde{P}_{\text{Tx}}\left(\vec{\mathbf{k}}_{xy},\hat{\mathbf{p}}_{\text{inc}}\right) * \tilde{\cos}\,\theta_{cell,Tx}\left(\vec{\mathbf{k}}_{xy}\right)\right]\right. \\
& \left[\tilde{f}_{\text{Rx}}\left(\vec{\mathbf{k}}_{xy}\right) * \tilde{P}_{\text{Rx}}\left(\vec{\mathbf{k}}_{xy},\hat{\mathbf{p}}_{\text{inc}}\right) * \tilde{\cos}\,\theta_{cell,Rx}\left(\vec{\mathbf{k}}_{xy}\right)\right] \\
& + \left[\tilde{f}_{\text{Tx}}\left(\vec{\mathbf{k}}_{xy}\right) * \tilde{P}_{\text{Tx}}\left(\vec{\mathbf{k}}_{xy},\hat{\mathbf{p}}_{\text{inc}}\right) * \tilde{\sin}\,\theta_{cell,Tx}\left(\vec{\mathbf{k}}_{xy}\right)\right] \\
& \left.\left[\tilde{f}_{\text{Rx}}\left(\vec{\mathbf{k}}_{xy}\right) * \tilde{P}_{\text{Rx}}\left(\vec{\mathbf{k}}_{xy},\hat{\mathbf{p}}_{\text{inc}}\right) * \tilde{\sin}\,\theta_{cell,Rx}\left(\vec{\mathbf{k}}_{xy}\right)\right]\right\}_{\text{LPF}}
\end{aligned} \tag{14}$$

and specifically, for the case that the aperture is used for both transmitting and receiving (i.e., full-duplex):

$$h\left(\vec{\mathbf{r}}'', \hat{\mathbf{p}}_{\text{inc}}\right) \propto \tilde{J}_{\text{m}}^2\left(\vec{\mathbf{k}}_{xy}\right) \propto \omega^2 \left\{ \left[\tilde{f}\left(\vec{\mathbf{k}}_{xy}\right) * \tilde{P}\left(\vec{\mathbf{k}}_{xy}, \hat{\mathbf{p}}_{\text{inc}}\right) * \tilde{\cos}\,\theta_{cell}\left(\vec{\mathbf{k}}_{xy}\right)\right]^2 + \left[\tilde{f}\left(\vec{\mathbf{k}}_{xy}\right) * \tilde{P}\left(\vec{\mathbf{k}}_{xy}, \hat{\mathbf{p}}_{\text{inc}}\right) * \tilde{\sin}\,\theta_{cell}\left(\vec{\mathbf{k}}_{xy}\right)\right]^2 \right\}_{\text{LPF}} \tag{15}$$

In Equations (14) and (15), h is formed by two sets of uncorrelated functions with $\tilde{\cos}\,\theta$ and $\tilde{\sin}\,\theta$ respectively, because $\tilde{P}$ varies with $\hat{\mathbf{p}}_{\text{inc}}$ given that the aperture elements are diversely polarized. The PD functions as a modulation to h via $\tilde{P}$. Combining with Equation (2), this additional diversity makes h vary with the polarization of illumination, hence it enables a potential of reducing the coherences in the measurements.

In order to highlight the significance of the PD, it is of interest to make a comparison between two h generated respectively by the apertures with and without the diversity. It is worth mentioning that conventional apertures also suit the no-polarization-diversity situation in this comparison even if they are not scattering apertures, because the difference in excitation modality does not alter the essential of the problem under discussion. In conventional configurations, the aperture elements are unitarily polarized, making θ_{cell} fixed to 0. This makes P equivalently independent of the illumination polarization, because the alteration of $\hat{\mathbf{p}}_{\text{inc}}$ only contributes to a factor that is ignorable due to its invariance in space:

$$\begin{aligned} &\tilde{\cos}\,\theta_{cell}\left(\vec{\mathbf{k}}_{xy}\right) = \delta\left(\vec{\mathbf{k}}_{xy}\right) \\ &\tilde{\sin}\,\theta_{cell}\left(\vec{\mathbf{k}}_{xy}\right) = 0 \\ &\tilde{P}\left(\vec{\mathbf{k}}_{xy}, \hat{\mathbf{p}}_{\text{inc}}\right) \propto \text{a const function of } \hat{\mathbf{p}}_{\text{inc}} \end{aligned} \tag{16}$$

For simplification of the comparison, consider the full-duplex situation. Combining with Equation (16), Equation (15) for conventional configurations degenerates to:

$$h\left(\vec{\mathbf{r}}''\right) \propto \omega^2 \left[\tilde{f}\left(\vec{\mathbf{k}}_{xy}\right) * \tilde{P}\left(\vec{\mathbf{k}}_{xy}\right)\right]^2_{\text{LPF}} \tag{17}$$

By comparison with Equation (13), Equation (15) shows that the two sets of uncorrelated functions degenerate when $\tilde{P}$ evolves to a function unrelated to $\hat{\mathbf{p}}_{\text{inc}}$. In other words, the additional degree of freedom in the generation of h disappears together with the PD.

As shown in Equations (14) and (15), $\tilde{P}$ plays an important role in the formulation of the PD. Therefore, in order to further illustrate the influence of the diversity, a numerical evaluation of $\tilde{P}$ is performed as follows: with the aim of simplifying the evaluation, the function P of a one-dimensional aperture that is composed of elements with polarization angles being randomly distributed in $[-\pi, \pi]$ is computed, while the weak-scattering assumption of elements is also adopted, hence making $H_{\text{inc}}^{\dagger}$ in Equation (9) an ignorable constant. Applying discrete Fourier transformation gives $\tilde{P}$ in matrix form, denoted as $\overline{\overline{P}}$, of which the row and column indexes respectively correspond to the k-space with the discrete number of M, and the polarization angles of illumination with the discrete number of N:

$$\overline{\overline{P}} := \begin{bmatrix} \tilde{P}\left(\vec{\mathbf{k}}_1^{xy}, \hat{\mathbf{p}}_1^{\text{inc}}\right) & \cdots & \tilde{P}\left(\vec{\mathbf{k}}_1^{xy}, \hat{\mathbf{p}}_N^{\text{inc}}\right) \\ \vdots & \ddots & \vdots \\ \tilde{P}\left(\vec{\mathbf{k}}_M^{xy}, \hat{\mathbf{p}}_1^{\text{inc}}\right) & \cdots & \tilde{P}\left(\vec{\mathbf{k}}_M^{xy}, \hat{\mathbf{p}}_N^{\text{inc}}\right) \end{bmatrix} \tag{18}$$

The polarization angle of illumination also varies within $[-\pi, \pi]$. Each column of $\overline{\overline{P}}$ corresponds to a function $\tilde{P}$ that is discrete in the k-space with a specific polarization of illumination. Since the column coherences of $\overline{\overline{P}}$ intuitively illustrate the additional diversity brought by the PD, as an indication of

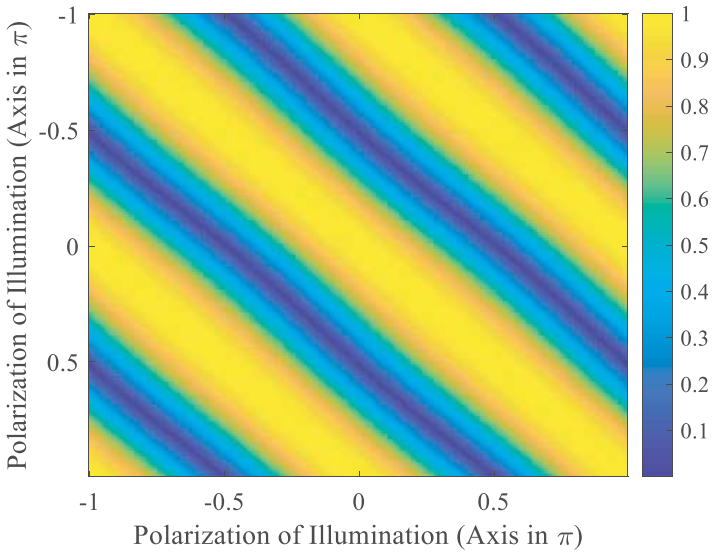

Figure 2. Amplitude of the Gramian matrix of $\overline{\overline{P}}$.

column coherences, the Gramian matrix of $\overline{\overline{P}}$ is evaluated with its amplitude being visualized as shown in Figure 2.

The Gramian matrix appears with a diagonal pattern, which indicates significant autocorrelation among the column vectors of $\overline{\overline{P}}$. Due to symmetry, a periodicity of π emerges in the diagonal pattern, which is in accordance with the conclusion in [14] that the maximum rotation angle reducing the mutual coherences in $\overline{\overline{H}}$ approximately saturates to 180 degrees. Obviously, $\overline{\overline{P}}$ evolves to an all-ones matrix when the element polarizations are aligned to one and the same direction, because in that case $\tilde{P}$ degenerates to a function that is constant in the k-space. Therefore, from the view of $\overline{\overline{P}}$'s coherence property, the PD of the elements makes $\tilde{P}$ vary and distinguish with each other when altering the polarization of illumination.

Before ending up this section, it is worth briefly discussing the limitation of the proposed formulation. Due to the presence of the convolutions in k-space, a further decomposition of Equations (14) and (15) seems to be quite difficult. Hence, it fails to isolate P and give an explicit formulation on how the mutual coherences in Equation (2) are reduced by introducing PD to aperture elements. However, the emergence of $\tilde{P}$ gives an additional degree of freedom in the generation of h, providing a potential of generating more incoherent h by making it vary with the polarization of illumination. From the view of spectral analysis, the new variable possesses the ability of expanding singular values and singular vectors of $\overline{\overline{H}}$. Although further analysis of Equations (14) and (15) is still needed, a coherence reduction by the PD will be observed in the following validation in the next section.

4. VALIDATION

In order to validate the proposed formulation, a set of comparisons between two sets of $\overline{\overline{H}}$ respectively generated by two cELC array apertures that is with or without the PD of aperture elements is implemented. These $\overline{\overline{H}}$ are numerically generated by the fields in the ROI according to Equation (1), while the fields are obtained via near-field scanning of the apertures in a microwave anechoic chamber. Equivalent magnetic currents of the apertures, average mutual coherences and singular value spectrum of $\overline{\overline{H}}$, and point spread function (PSF) as an imaging evaluation, are respectively observed with the PD and imaging range being two independent variables. The experimental setup and the results are elaborated as follows.

4.1. Experimental Setup

A 400 mm ∗ 400 mm "random dual-polarizations" cELC array is fabricated as a testing aperture. As shown in Figure 3, this aperture is in common with a typical cELC array that is composed of weak-coupling radiating elements with resonant frequencies determined primarily by the length of the slit in the middle of the element [9], but is also distinguished by the random vertical/horizontal polarizations of the elements. The resonant frequencies of the elements are randomly selected within the range from 27.5 GHz to 34 GHz, while the polarizations are also randomly selected between vertical and horizontal.

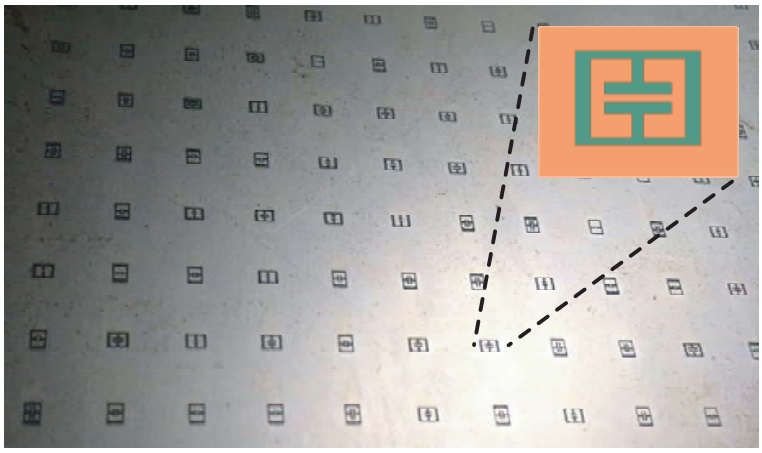

Figure 3. Enlarged view of the cELC array composed of cELC elements with random dual-polarizations. The polarization is randomly configured to vertical or horizontal.

For comparison, we also fabricate a conventional cELC array aperture, of which every configuration is completely identical to the testing one, except the polarizations of elements: all the elements of this aperture are placed vertically, i.e., unitarily polarized.

As a scattering aperture, the two arrays are sequentially placed in a microwave anechoic chamber under the illumination of an open-ended waveguide (OEWG), which is placed a few meters away from the aperture as a generator of plane waves. A near-field probe scans on the other side of the aperture (backside of the illumination). The schematic diagram and actual scenario are shown in Figures 4(a) and (b), respectively. For each aperture, we perform two scannings, while in each scanning the polarization of the OEWG is set to vertical or horizontal in sequence. Therefore, the only difference between the scannings of the two apertures is the polarization configuration of aperture elements.

Figure 4. Near-field scanning in a microwave anechoic chamber: (a) schematic diagram; (b) actual scenario.

A frequency sweep is performed from 27.5 GHz to 34 GHz with the interval of 200 MHz. The interval of the spatial scanning is 4 mm, which satisfies the requirement of Nyquist sampling at the frequency of 34 GHz.

With the consideration of reducing the interference of the diffraction from the edges and shortening the scanning time, the scanning area is set to a 200 mm∗200 mm square at the center of the aperture and a few millimeters away from the surface. According to surface equivalence theorem, the fields radiated by the aperture can be yielded by the equivalent magnetic currents in the scanning plane S, i.e., the cross product of the normal vector $\hat{\mathbf{n}}$ and the tangent electric field measured by the probe $\vec{\mathbf{E}}_{\text{prob}}$:

$$\vec{\mathbf{E}}_{\text{inc}}\left(\vec{\mathbf{r}}''\right) = \int_S \nabla'' G_0\left(\vec{\mathbf{r}}'', \vec{\mathbf{r}}'\right) \times \left[\hat{\mathbf{n}} \times \vec{\mathbf{E}}_{\text{prob}}\left(\vec{\mathbf{r}}'\right)\right] \mathrm{d}^2\vec{\mathbf{r}}' \tag{19}$$

where G_0 is Green's function in free space. In this validation, the aperture is configured in full-duplex mode for simplification of setup. Therefore, a row of $\overline{\overline{H}}$ can be numerically generated by the square of the electric field in the ROI: E_{inc}^2, at a discrete point of the frequency sweep, according to Equation (1). The ROI is set to a square with the same size of the scanning area, while the square and the area are coaxial as shown in Figure 1, and the imaging range z varies.

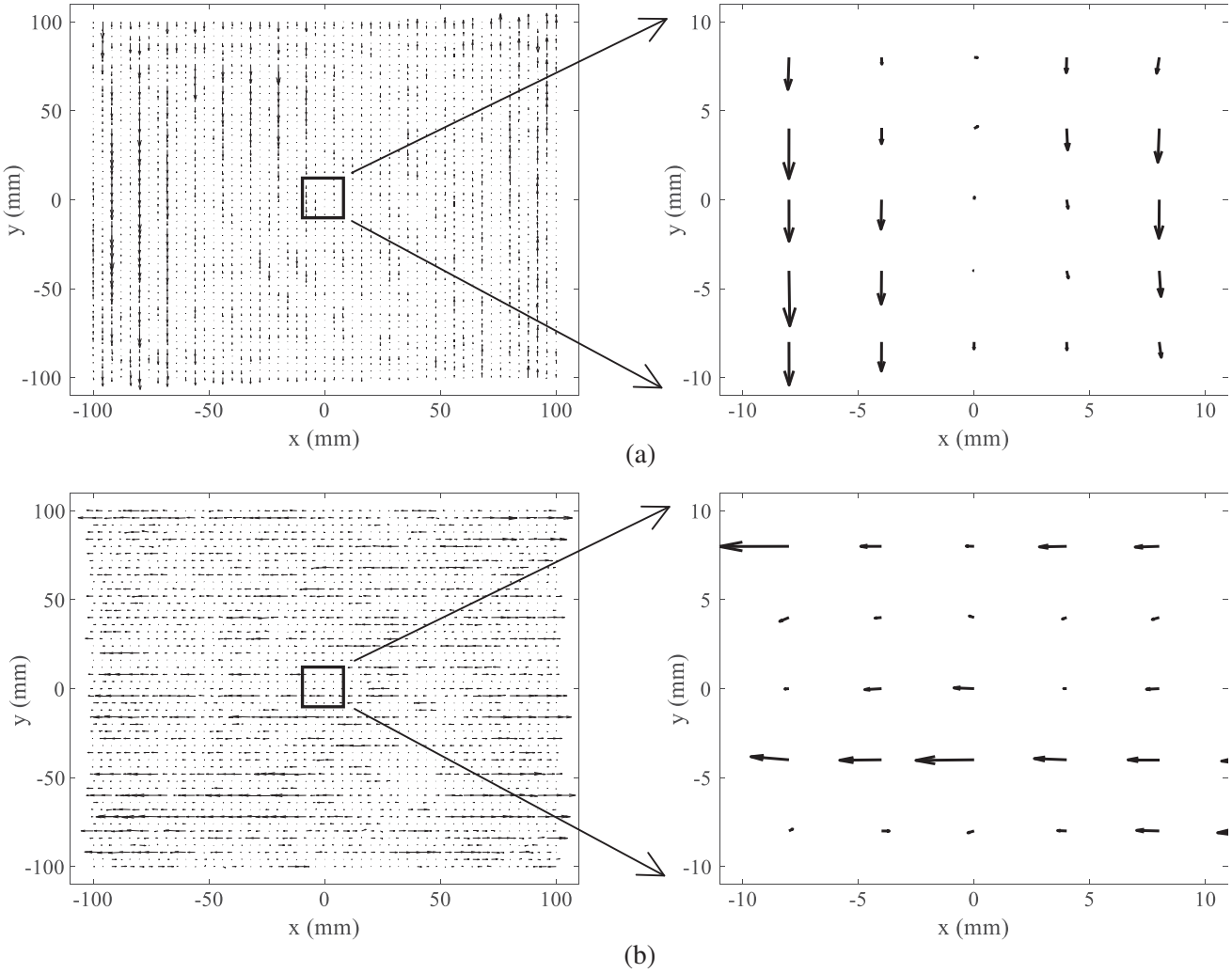

Figure 5. Equivalent magnetic current of the randomly dual-polarized aperture stimulated by an incident plane field with (a) vertical polarization, and (b) horizontal polarization, respectively. The diagrams on the right are the magnified views of the currents at the center.

5. RESULTS

Firstly, a comparison of the equivalent magnetic currents is performed. A pair of vector diagrams of the testing aperture's equivalent magnetic current at the frequency of 30 GHz under the illuminations of vertical and horizontal polarization respectively is shown in Figure 5.

The result shows that the polarization of the magnetic current is basically in the same direction with the polarization of illumination, validating that the magnetic susceptibility tensor of the elements is diagonal. The intensities of the currents under illuminations with different polarizations demonstrate obvious differences in spatial distribution. The spatial diversity of the magnetic currents implies a potential of increasing diversity in the measurements.

Next, the electric fields are propagated to the ROI according to Equation (19), giving a frequency-sweep based $\overline{\overline{H}}$. As a convenient indicator, the average mutual coherence μ_{g} [26]:

$$\mu_{\mathrm{g}} = \frac{\sum\limits_{i \neq j} \left| \left[\hat{\overline{\overline{\mathbf{H}}}}^{*} \hat{\overline{\overline{\mathbf{H}}}} \right]_{ij} \right|^2}{N_{\mathrm{ROI}} \left(N_{\mathrm{ROI}} - 1 \right)} \tag{20}$$

is observed to evaluate the coherence level of $\overline{\overline{H}}$ (N_{ROI} is the number of discrete grids in the ROI), while the varying range serves as an independent variable, as shown in Figure 6.

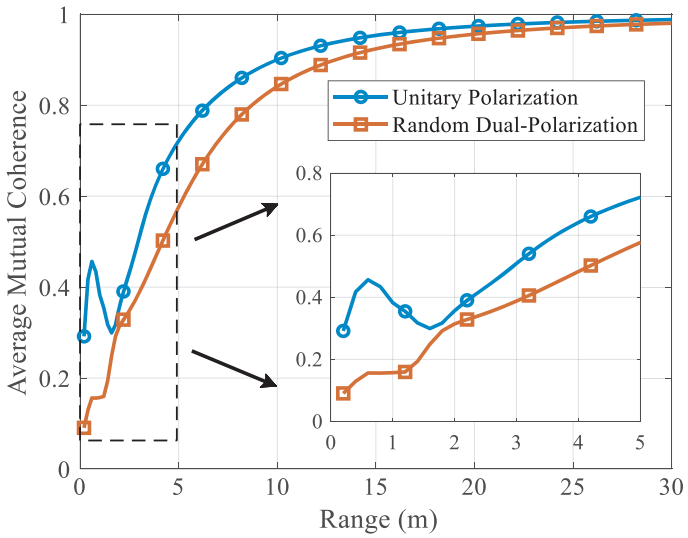

Figure 6. Comparison of the average mutual coherences of the measurement matrices respectively generated by the unitarily polarized aperture and randomly dual-polarized aperture.

The significant gap between the two curves shows that the coherence level of $\overline{\overline{H}}$ is obviously reduced by the PD of aperture elements. More specifically, in the near-field region, the reduction of the coherences is very explicit, while with the increasing of imaging range, in the far-field region, the coherence level increases, and the reduction becomes relatively insignificant. The trend of the coherences growing with the increase of imaging range coincides with the shrinking spectral low-pass filter yielded by the AOV [3]. Figure 6 validates that the additional degree of freedom brought by the PD reduces the mutual coherences in $\overline{\overline{H}}$, while the benefit is subject to the finite AOV.

Finally, singular value decomposition is applied to $\overline{\overline{H}}$ at the imaging range of 0.2 m and 2.0 m, respectively, giving the singular spectrum of the matrices as shown in Figure 7. "Uni" and "Rnd" in the legend denote the unitarily polarized aperture and the testing aperture, respectively. At the range of 0.2 m, the singular spectrum of the testing aperture is significantly improved compared with the "Uni"

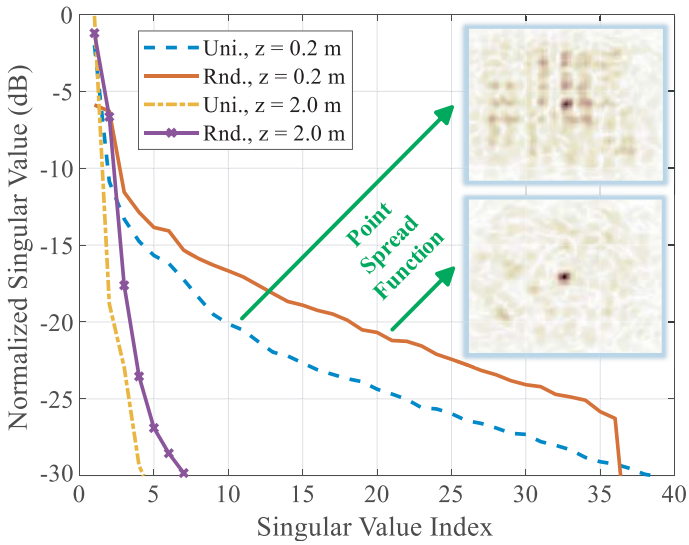

Figure 7. Comparisons of the singular spectra and the PSFs. "Uni" and "Rnd" denote the unitarily polarized and randomly dual-polarized aperture respectively, while z is the imaging range. The subplot at the upper right corner is the comparison of the PSFs respectively generated by the two apertures at the range of 0.2 m with the SNR of 30 dB. The reconstruction algorithm is TwIST.

one, while at the range of 2.0 m, the improvement is still discernable but less significant. The comparison of the singular spectrum proves that the effective singular values and corresponding singular vectors can be expanded by the PD of aperture elements. The improvement of singular system corroborates to the coherence reduction.

In order to visualize the improvement brought by the PD, PSF, which is the reconstruction of a point object in the center of the ROI, is generated by implementing virtual imaging experiment with the $\overline{\overline{H}}$ at the imaging range of 2.0 m (in correspondence to the singular spectrum at the same range, as shown in Figure 7). The experiment is implemented with a signal-to-noise ratio (SNR) of 30 dB. Since the matrix equation of Equation (1) for the imaging scenario is very underdetermined, a compressed-sensing based reconstruction algorithm, TwIST [27], is implemented for the inversion. The results are shown at the upper right corner of Figure 7. Although the spatial resolutions of the PSFs are almost identical, the emergence of speckles with the PSF of the unitarily polarized aperture shows that the ill-posedness is significantly worse than the PSF of the testing aperture, indicating that the reconstruction performance of $\overline{\overline{H}}$ is improved by the PD.

In summary, the comparisons of coherence level, singular spectrum, and PSF of $\overline{\overline{H}}$ validate that the PD of aperture elements is capable of reducing the mutual coherences in the measurements and thus improves the reconstruction performance of MCI.

6. CONCLUSIONS

An electromagnetic formulation of the PD of scattering aperture elements on the measurement matrix's coherence reduction is presented. The PD gives a new degree of freedom in the generation of the measurements, which effectively reduces the coherences in the measurement matrix given illuminations with varying polarizations. The improvement brought by the PD weakens with the increasing of imaging range. The proposed formulation is validated by the near-field scanning of two cELC apertures with and without the PD respectively.

ACKNOWLEDGMENT

This work was supported by the National Natural Science Foundation of China, No. 61431016.

REFERENCES

1. Mait, J. N., G. W. Euliss, and R. A. Athale, "Computational imaging," *Advances in Optics and Photonics*, Vol. 10, 409–483, 2018.
2. Yurduseven, O., T. Fromenteze, K. Cooper, G. Chattopadhyay, and D. R. Smith, "From microwaves to submillimeter waves: Modern advances in computational imaging, radar, and future trends," *Proceedings of Society of Photographic Instrumentation Engineers*, Vol. 10917, San Francisco, United States, Feb. 2–7, 2019.
3. Guan, J. and W. Chen, "On the coherence relationship between measurement matrices and equivalent radiation sources in microwave computational imaging applications," *Applied Sciences*, Vol. 9, 1172, 2019.
4. Huang, K. and X. Zhao, *Inverse Problems in Electromagnetic Fields and Its Applications*, 1st Edition, Science Press, Beijing, China, 2005 (in Chinese).
5. Gureyev, T. E., D. M. Paganin, A. Kozlov, Ya. I. Nesterets, and H. M. Quiney, "Complementary aspects of spatial resolution and signal-to-noise ratio in computational imaging," *Physical Review A*, Vol. 97, 053819, 2018.
6. Carin, L., D. Liu, and B. Guo, "Coherence, compressive sensing, and random sensor arrays," *IEEE Antennas and Propagation Magazine*, Vol. 53, 28–39, 2011.
7. Hunt, J., T. Driscoll, A. Mrozack, G. Lipworth, M. Reynolds, D. Brady, and D. R. Smith, "Metamaterial apertures for computational imaging," *Science*, Vol. 339, 310–313, 2013.
8. Lipworth, G., A. Mrozack, J. Hunt, D. L. Marks, T. Driscoll, D. Brady, and D. R. Smith, "Metamaterial apertures for coherent computational imaging on the physical layer," *Journal of Optical Society of America A*, Vol. 30, 1603–1612, 2013.
9. Hunt, J., J. Gollub, T. Driscoll, G. Lipworth, A. Mrozack, M. S. Reynolds, D. J. Brady, and D. R. Smith, "Metamaterial microwave holographic imaging system," *Journal of Optical Society of America A*, Vol. 31, 2109–2119, 2014.
10. Fromenteze, T., O. Yurduseven, M. F. Imani, J. Gollub, C. Decroze, D. Carsenat, and D. R. Smith, "Computational imaging using a mode-mixing cavity at microwave frequencies," *Applied Physics Letters*, Vol. 106, 194104, 2015.
11. Imani, M. F., T. Sleasman, J. N. Gollub, and D. R. Smith, "Analytical modeling of printed metasurface cavities for computational imaging," *Journal of Applied Physics*, Vol. 120, 144903, 2016.
12. Marks, D. L., J. Gollub, and D. R. Smith, "Spatially resolving antenna arrays using frequency diversity," *Journal of Optical Society of America A*, Vol. 33, 899–912, 2016.
13. Sleasman, T., M. F. Imani, J. N. Gollub, and D. R. Smith, "Dynamic metamaterial aperture for microwave imaging," *Applied Physics Letters*, Vol. 107, 204104, 2015.
14. Wu, Z., L. Zhang, H. Liu, and N. Kou, "Enhancing microwave metamaterial aperture radar imaging performance with rotation synthesis," *IEEE Sensors Journal*, Vol. 16, 8035–8043, 2016.
15. Yoya, A. C. T., B. Fuchs, C. Leconte, and M. Davy, "A reconfigurable chaotic cavity with fluorescent lamps for microwave computational imaging," *Progress In Electromagnetics Research*, Vol. 165, 1–12, 2019.
16. Zhu, S., X. Dong, Y. He, M. Zhao, G. Dong, X. Chen, and A. Zhang, "Frequency-polarization-diverse aperture for coincidence imaging," *IEEE Microwave and Wireless Components Letters*, Vol. 28, 82–84, 2018.
17. Poon, A. and D. Tse, "Polarization degrees of freedom," *Proceedings of 2008 IEEE International Symposium on Information Theory*, 1587–1591, Toronto, Canada, Jul. 6–11, 2008.
18. Chew, W.-C., *Waves and Fields in Inhomogeneous Media*, 1st Edition, IEEE Press, New York, United States, 1995.
19. Van Den Berg, P. M. and R. E. Kleinman, "A contrast source inversion method," *Inverse Problems*, Vol. 13, 1607–1620, 1997.

20. Sleasman, T., M. Boyarsky, M. F. Imani, J. N. Gollub, and D. R. Smith, "Design considerations for a dynamic metamaterial aperture for computational imaging at microwave frequencies," *Journal of Optical Society of America B*, Vol. 33, 1098–1111, 2016.
21. Hori, M., "Inverse analysis method using spectral decomposition of Green's function," *Geophysical Journal International*, Vol. 147, 77–87, 2001.
22. Kastner, R., "On the singularity of the full spectral Green's dyad," *IEEE Transactions on Antennas and Propagation*, Vol. 35, 1303–1305, 1987.
23. Pellat-Finet, P., "Fresnel diffraction and the fractional-order Fourier transform," *Optics Letters*, Vol. 19, 1388–1390, 1994.
24. Alieva Vicente Lopez, T., F. Agullo-Lopez, and L. B. Almeida, "The fractional Fourier transform in optical propagation problems," *Journal of Modern Optics*, Vol. 41, 1037–1044, 1994.
25. Ledger, P. D. and W. R. Bill Lionheart, "Understanding the magnetic polarizability tensor," *IEEE Transactions on Magnetics*, Vol. 52, 1–16, 2016.
26. Duarte-Carvajalino, J. M. and G. Sapiro, "Learning to sense sparse signals: Simultaneous sensing matrix and sparsifying dictionary optimization," *IEEE Transactions on Image Processing*, Vol. 18, 1395–1408, 2009.
27. Bioucas-Dias, J. M. and M. A. T. Figueiredo, "A new TwIST: Two-step iterative shrinkage/thresholding algorithms for image restoration," *IEEE Transactions on Image Processing*, Vol. 16, 2992–3004, 2007.